Crystal structures of bacterial peptidoglycan amidase AmpD and an unprecedented activation mechanism

César Carrasco-López, Alzoray Rojas-Altuve, Weilie Zhang, Dusan Hesek, Mijoon Lee, Sophie Barbe, Isabelle André, Pilar Ferrer, Noella Silva-Martin, German R. Castro, et al.

THE JOURNAL OF BIOLOGICAL CHEMISTRY VOL. 286, NO. 36, pp. 31714–31722, September 9, 2011

Crystal Structures of Bacterial Peptidoglycan Amidase AmpD and an Unprecedented Activation Mechanism*[S]

Received for publication, May 24, 2011, and in revised form, June 28, 2011 Published, JBC Papers in Press, July 20, 2011, DOI 10.1074/jbc.M111.264366

Cesar Carrasco-López[‡1], Alzoray Rojas-Altuve[‡], Weilie Zhang[§], Dusan Hesek[§], Mijoon Lee[§], Sophie Barbe[¶], Isabelle André[¶], Pilar Ferrer[‖], Noella Silva-Martin[‡], German R. Castro[‖**], Martín Martínez-Ripoll[‡], Shahriar Mobashery[§2], and Juan A. Hermoso[‡3]**

*From the [‡]Departamento de Cristalografía y Biología Estructural, Instituto de Química-Física "Rocasolano", CSIC, Serrano 119, 28006 Madrid, Spain, the [§]Department of Chemistry and Biochemistry, 423 Nieuwland Science Center, University of Notre Dame, Notre Dame, Indiana 46556, the [¶]INSA, UPS, INP, LISBP, 135 Avenue de Rangueil, F-31077 Toulouse, France, CNRS, UMR5504, F-31400 Toulouse, France, the INRA, UMR792 Ingénierie des Systèmes Biologiques et des Procédés, Université de Toulouse, F-31400 Toulouse, France, the [‖]SpLine Spanish CRG beamline at the European Synchrotron Radiation Facility 6 rue Jules Horowitz, F-38043 Grenoble, France, and the **Instituto de Ciencia de Materiales de Madrid (ICMM-CSIC), Cantoblanco, 28049 Madrid, Spain*

AmpD is a cytoplasmic peptidoglycan (PG) amidase involved in bacterial cell-wall recycling and in induction of β-lactamase, a key enzyme of β-lactam antibiotic resistance. AmpD belongs to the amidase_2 family that includes zinc-dependent amidases and the peptidoglycan-recognition proteins (PGRPs), highly conserved pattern-recognition molecules of the immune system. Crystal structures of *Citrobacter freundii* AmpD were solved in this study for the apoenzyme, for the holoenzyme at two different pH values, and for the complex with the reaction products, providing insights into the PG recognition and the catalytic process. These structures are significantly different compared with the previously reported NMR structure for the same protein. The NMR structure does not possess an accessible active site and shows the protein in what is proposed herein as an inactive "closed" conformation. The transition of the protein from this inactive conformation to the active "open" conformation, as seen in the x-ray structures, was studied by targeted molecular dynamics simulations, which revealed large conformational rearrangements (as much as 17 Å) in four specific regions representing one-third of the entire protein. It is proposed that the large conformational change that would take the inactive NMR structure to the active x-ray structure represents an unprecedented mechanism for activation of AmpD. Analysis is presented to argue that this activation mechanism might be representative of a regulatory process for other intracellular members of the bacterial amidase_2 family of enzymes.

Bacterial cell wall is comprised of cross-linked strands of peptidoglycan (PG),[4] which encase the entire cytoplasm. A healthy cell wall is critical for survival of bacteria. During homeostasis, including growth, cell wall is simultaneously biosynthesized and degraded (1). In the course of the normal bacterial growth, more than 50% of the parental peptidoglycan is recycled (1, 2). Whereas the biosynthesis has been studied in greater detail, the degradation of cell wall is less understood, yet it is believed to be quite important. Degradation sets in motion the process of recycling of cell-wall components.

Lytic transglycosylases initiate the degradative events on cell wall (Fig. 1*A*) in a manner that forms and releases a special disaccharide natural product, compound **1**, which is internalized by the function of the integral membrane protein AmpG (3). Once in the cytoplasm, the reaction of NagZ on **1** removes the *N*-acetylglucosamine moiety resulting in compound **2**, which then serves as the substrate for AmpD, the second enzyme in the cell-wall recycling pathway. The hydrolytic reaction of AmpD cleaves the peptide from the l-lactyl moiety of **2** resulting in fragments **3** and the peptide **4** (4). The reaction products of NagZ and AmpD play roles in both the entry into the ensuing peptidoglycan recycling events and in an induction event that leads to the expression of β-lactamase, a key β-lactam antibiotic resistance enzyme (5, 6).

AmpD belongs to the amidase_2 family (PF01510) that includes zinc amidases from different pathogenic species (*e.g. Mycobacterium tuberculosis, Streptococcus pneumoniae, Staphylococcus aureus,* and *Clostridium botulinum* among others) and all of the peptidoglycan-recognition proteins (PGRPs). PGRPs are pattern-recognition proteins that bind and, in certain cases, hydrolyze PG of bacterial cell walls (7–9). PGRPs are found in both invertebrates and vertebrates, but have developed different functions in different animals. Insect PGRPs are involved in the Toll receptor and Imd-signaling pathways that induce expression of antimicrobial peptides (10–12). By contrast, mammalian PGRPs do not act through host signaling pathways, but are bactericidal (11, 13, 14).

* This work was supported, in whole or in part, by the National Institutes of Health. This work was also supported by grants from the Spanish Ministry of Science and Technology (BFU2008-01711), EU-CP223111 (CARE-PNEUMO, European Union), and the COMBACT program (S-BIO-0260/2006). We acknowledge the Spanish Ministerio de Ciencia e Innovación (PI201060E013) and Consejo Superior de Investigaciones Científicas for financial support and for provision of synchrotron radiation facilities.

The atomic coordinates and structure factors (codes 2y28, 2y2d, 2y2c, 2y2b, and 2y2e) have been deposited in the Protein Data Bank, Research Collaboratory for Structural Bioinformatics, Rutgers University, New Brunswick, NJ (http://www.rcsb.org/).

[S] The on-line version of this article (available at http://www.jbc.org) contains supplemental Tables S1 and S2, Figs. S1–S7, and Movies S1 and S2.

[1] A fellow of the Fundayacucho Foundation (Venezuela).

[2] To whom correspondence may be addressed: Serrano, 119, 28006 Madrid, Spain. Tel.: 34-915619400; Fax: 34-915642431; E-mail: xjuan@iqfr.csic.es.

[3] To whom correspondence may be addressed: 423 Nieuwland Science Center, IN 46556. E-mail: mobashery@nd.edu.

[4] The abbreviations used are: PG, peptidoglycan; PGRP, peptidoglycan-recognition protein; TMD, Targeted Molecular Dynamics; RMSD, root mean square deviation; XAS, x-ray absorption spectroscopy; EXAFS, extended x-ray absorption fine structure.

The NMR structure of *Citrobacter freundii* AmpD has been reported (15) and its fold together with coordination of the catalytic zinc ion have been described. However, this structure did not provide information about substrate binding or mechanism of hydrolysis. We report herein the first x-ray structure for AmpD, as well as its complex with its reaction products. As is outlined in this report, the x-ray structure(s) represent the active conformer of the enzyme. Indeed, we show that the crystals are catalytically active, resulting in the two products on soaking of substrate **2.** These x-ray structures for AmpD were contrasted with the previously reported NMR structure. The NMR folding does not possess an accessible active site and shows the protein in what we characterize as an inactive "closed" conformation. The transition of the protein from this inactive conformation to the active "open" conformation entails large conformational changes of as much as 17 Å. We believe that the degree of this conformational change is unprecedented for any single-domain protein. We put forward a proposal that this large conformational change represents a novel regulatory mechanism for activation of this metalloprotease, which does not find precedent in the considerable literature of these hydrolytic enzymes.

EXPERIMENTAL PROCEDURES

AmpD Substrates Synthesis—The substrates for AmpD, compounds 1 and 2, were synthesized according to the literature (16).

AmpD Production and Seleno-methionine Labeling of AmpD in Escherichia coli—The AmpD gene was cloned from *C. freundii* and ligated into pET24a(+) vector under the T7 promoter, as described before (4). We used the methionine auxotrophic *E. coli* B834 (DE3) for transformation with the plasmid. Initially cells were grown in minimal medium containing all essential amino acids. After cell growth reached mid-log phase (12–18 h), the cells were spun down, and the pellet was resuspended in the minimal medium (without methionine). The cells were starved by incubating for 8–12 h at 37 °C, before the addition of seleno-L-methionine. The overexpression of AmpD was induced by IPTG (400 μM) to allow incorporation of seleno-L-methionine. The incorporation of seleno-methionine into purified AmpD was confirmed by mass spectrometry.

Preparation of Bacterial Lipid Extract Vesicles—Lipid vesicles were prepared to test the activity of AmpD in their presence. Chloroform in lipid (*E. coli* Lipid Extract, Avanti Polar Lipid, Inc.) stock solutions (25 mg/ml) was removed under a flow of nitrogen and the residue was resuspended in a flow buffer solution (10 mM HEPES, pH 7.4, containing 0.16 M KCl). The solution was then mixed for 5 min and submitted to sonification for 10 min in a Branson 1200 sonifier. After sonification, lipid solutions were passed 17 times through a Liposofast microextruder containing a 400 nm polycarbonate filter. Lipids concentration was 15 mg/ml, the final concentration of total lipids was 1.5 mg/ml in reaction buffer.

Kinetic Studies—The assays were carried out in 20 mM sodium phosphate buffer, 1.0 mM DTT, pH 7.0 or 40 mM bicarbonate buffer, 1.0 mM DTT, pH 7.0, at 25 °C with substrate (anhMurNAc-tripeptide; compound **2**) concentrations ranging from 100 μM to 3.0 mM and AmpD concentrations of 50 nM. The reaction mixtures were incubated at 25 °C for 30 min in the absent or present of lipids. The reactions were stopped by the addition of 2 volume of 0.1% TFA in water. Reaction products were separated and quantified on a C18 reversed-phase HPLC column (Sunfire C18, 3.5 μm, 4.6 mm × 150 mm; Waters) on a PerkinElmer series 200 System. The column was equilibrated with 0.05% trifluoroacetic acid in water and eluted with a linear acetonitrile gradient from 0 to 15% over 40 min with a flow rate of 1 ml/min. The column effluent was monitored at 205 nm. The catalytic activity of the AmpD was quantified from the rate of substrate disappearance and of tripeptide appearance.

Crystallization—High-throughput techniques with a NanoDrop™ ExtY robot (Innovadyne Technologies Inc.) were carried out to test initial crystallization assays based on commercial Qiagen screenings, JCSG+Suite and PACT Suite. All crystallization nano-trials were performed by sitting-drop vapor-diffusion method at 291 K on Innovaplate™ S.D.-2 microplates (Innovadyne Technologies Inc.) mixing equal amounts (250 nl) of purified AmpD (17 mg/ml in 50 mM Na_2HPO_4, pH 7.0, supplemented with 1 mM NaN_3) and precipitant solutions. NanoDrop robot drops (500 nl, protein and precipitant solutions) were equilibrated against 65 ml of mother liquor. Good quality crystals of AmpD and AmpD-SeMet grew under conditions containing 0.1 M Tris, pH 6.0, 0.1 M Li_2SO_4 plus 28% PEG 3350, using the sitting drop method (1:1 volume proportion), mixing 1 μl of native AmpD (or 1 μl of AmpD-SeMet) at 8 mg/ml in 20 mM Na_2HPO_4, pH 7.0, 1 mM DTT, 1 mM NaN_3, with 1 μl of precipitant solution and equilibrated against 500 μl of mother liquor. AmpD complexes were prepared using holoenzyme crystals; these crystals were soaked rapidly into mother liquor supplemented with 25% of glycerol and 50 mM compound **2**.

X-ray Data Collection and Structural Determination—AmpD-SeMet crystals were soaked for 5 s in a cryoprotectant solution (20% v/v of glycerol diluted in crystallization mother liquor) prior to flash-cooling at 100 K. X-ray data sets up to 1.7 Å resolution were collected using synchrotron radiation facility at ESRF (Grenoble). Multiple-wavelength anomalous diffraction (MAD) data sets from AmpD-SeMet crystals were collected at 100 K on BM14 beamline using Marmosaic 225 CCD detector (oscillation range 1°, crystal-detector distance set to 169.26 mm). Holoenzyme, apoenzyme, AmpD-complex and AmpD at pH 5.5 data sets were collected at 100 K on ID14-1 (apoenzyme, AmpD-complex), ID29 (holoenzyme) and ID23–2 (AmpD at pH 5.5) beamlines. All data sets were processed using XDS (17) and MOSFLM (18) and scaled using SCALA (19) from CCP4 program suite (20). Data processing results are summarized in Table 1. Auto-Rickshaw (21) MAD procedure was used (three-wavelengths) to phase and build an initial model. Five selenium atom positions were found for the three molecules present in the asymmetric unit. The occupancy of all substructure atoms was refined, and initial phases were calculated using the program MLPHARE (20). Electron density maps were improved using the DM program (22), followed by automatic auto-tracing of three monomers in the asymmetric unit, using program ARP/warp (23). A total of 320 residues (out of 561) were automatically assigned in the asymmetric unit and the remaining residues were modeled manually using the pro-

gram O (24) and COOT (25). Structural model was refined with the PHENIX program (26). The holoenzyme, apoenzyme, the AmpD complex, and AmpD at pH 5.5 were solved by the molecular replacement method with the program MolRep from CCP4 (20), using AmpD-SeMet model as the initial template. Refinement of these structures was carried out with the PHENIX program (26). The final models presented good stereochemistry parameters and R and R_{free} values (Table 1).

Targeted Molecular Dynamics Calculations—The conformational transitions from the closed to the open AmpD conformers were simulated using the Targeted Molecular Dynamics (TMD) method implemented in AMBER 9 suite of programs. The models of AmpD were derived from the corresponding coordinates of the closed NMR structure (PDB accession code: 1J3G) and the high-resolution crystal structure of AmpD in its open conformation. Hydrogen atoms were added on histidine side chains based on protonation scheme derived from NMR analysis. Histidines 34, 61, 75, and 96 and 154 were only protonated at Ne whereas charged histidines 18 and 69 were protonated at both nitrogens, Nδ and Ne. The all-atom ff03 force field (27, 28), with the Generalized Born/Surface Area solvation model was used in TMD simulations (29). Preparation of simulations consisted of 6 initial energy minimization cycles (200 steps of steepest descent followed by 500 steps of conjugate gradient methods), where atomic positions of the protein backbone were restrained using a harmonic potential. The force constant was progressively diminished along the energy-minimization procedure from 20 to 1 kcal mol^{-1} $Å^{-2}$. A slow heating to 303 K over a period of 20 ps followed the energy minimizations, while restraining backbone atoms using a harmonic potential of 10 kcal mol^{-1} $Å^{-2}$. At the final required temperature, the system was equilibrated for 80 ps, while progressively decreasing the harmonic restraints on backbone atoms from 10 to 1 kcal mol^{-1} $Å^{-2}$. Finally, an unrestrained equilibration was performed over 20 ps. Langevin dynamics were used to maintain the temperature at 303 K. Long-range electrostatic forces were handled by the particle-mesh Ewald method. The time step of the simulations was 2.0 fs, and the SHAKE algorithm was used to constrain the lengths of all chemical bonds involving hydrogen atoms to their equilibrium values.

The TMD method allows observing large scale conformational transitions between two known end point conformations of a protein, which are presently beyond the reach of atomistic MD simulations. This is accomplished by an additional steering force based on a mass-weighted RMSD with respect to reference target conformation that is applied in the force field as an extra harmonic potential energy term of the form in Equation 1,

$$E = 0.5\ \mathrm{kr} \times \mathrm{N} \times (\mathrm{RMSD}(t) - \mathrm{taRMSD}(t))^2 \qquad \text{(Eq. 1)}$$

where E is the biasing potential energy in kcal/mol during the TMD simulation, kr is the force constant, N is the number of atoms, RMSD(t) is the root mean square deviation of the simulation structure at time t relative to the target structure and taRMSD(t) is the target RMSD value at time t. The conformational transition from the initial geometry to the final target geometry is driven by decreasing the value of the tRMSD(t) to 0 as a function of the simulation time. A force constant of 0.04–0.06 kcal mol^{-1} $Å^{-2}$ applied on heavy atoms of the protein over 1 ns appeared sufficient to find a path for the transition.

The resulting trajectories were analyzed using the Ptraj module of the AMBER package (30). The RMSD was calculated for the protein backbone atoms using least squares fitting. Distances between given residues were calculated with respect to their center of mass.

X-ray Absorption Spectroscopy—X-ray absorption spectroscopy (XAS) measurements were performed at the Spanish CRG beamline (SpLine-BM25-A) at the ESRF (31). XAS spectra recorded at Zn K-edge on AmpD protein were measured under several experimental conditions: crystalline protein suspended in pH 6 solution and AmpD solutions at pH 5.6, 7, and 8.2. The samples were placed on quartz capillary and/or a Teflon special cell sealed by Kapton film depending on the solution concentration and quantity. The XAS spectra have been recorded at room temperature. Several scans for each sample were carried out to check the sample stability along the time and to improve the signal-to-noise ratio. The incoming beam was monitored by a N_2-filled ionization chamber. Data were collected in the fluorescence yield mode with a 13-element Si(Li) energy dispersive detector (from e2v Instruments). XAS data for crystalline protein suspended on pH 6 solution were measured up to k = 15 and for AmpD solutions at different pH values up to k = 12. Zn-KA fluorescence line was recorded with the detector placed parallel to the x-ray electric polarization field (*i.e.* forming 90° from the incoming x-ray beam). Data treatment was with ATHENA software and EXAFS analysis was performed with ARTEMIS fitting software (32). The Fourier transforms were obtained from the EXAFS signal using a Hanning window between 2.5–10, 2.6–7.8, 2.6–8.8, and 2.4–8.4 $Å^{-1}$ for crystalline and liquid solutions at 5.6, 7, and 8.2 pH, respectively. The filtered EXAFS signals, resulting from Fourier transformation from the experimental signal, were obtained using a Hanning window between 1.0 and 3.3 Å. Scattering amplitudes and phase functions of the coordination spheres were calculated from AmpD x-ray crystal structure, with the FEFF6 code (33).

RESULTS AND DISCUSSION

Overview of the Crystal Structure of AmpD—Crystal structure of AmpD was solved by MAD technique with a Se-Met derivative, as molecular replacement failed when NMR structure was used as initial model. High-resolution crystal structures for a Se-Met derivative of AmpD, the holoenzyme, the apoenzyme, and the complex with the reaction products have been solved in this report (Table 1). Superimposition of all these structures yields an average root mean square deviation (RMSD) value of 0.14 Å. The crystal structure of AmpD presents a fold related to that of PGRPs and T7 lysozyme, and comprises three β-sheets, four α-helices and four 3-helical turns (Fig. 1*B*). Superimposition with the previously reported NMR structure for the same enzyme (15) revealed a very high RMSD value of 3.9 Å for all (181) Cα atoms. The highest observed deviations (4 to 17 Å) are concentrated in four specific regions of the protein (r1, residues 17–26; r2, residues 38–71; r3, residues 120–124 and r4, residues 158–165), representing one-third of the entire protein (Fig. 2 and supplemental Movie S1).

TABLE 1
Data collection and refinement statistics

Parameters		AmpD-SeMet		Holoenzyme	Apoenzyme	AmpD-complex	AmpD-pH 5.5
Data collection							
Space group		$P3_2$		$P3_2$	$P3_2$	$P3_2$	$P3_2$
Cell dimensions							
a, *c* (Å)		67.7, 92.7		67.7, 92.8	68.08, 93.08	67.7, 92.8	67.98, 93.12
α, b, γ (°)		90, 90, 120		90, 90, 120	90, 90, 120	90, 90, 120	90, 90, 120
T (K)		100		100	100	100	100
	Peak	*Inflection*	*Remote*				
Wavelength (Å)	0.97856	0.978910	0.918400	0.97625	0.93340	0.97627	0.872600
Resolution (Å)	1.8	1.85	1.7	2.0	1.8	1.9	2.0
No. unique reflections	42215	39677	52405	32155	44523	31507	32782
R_{merge} (%)	8.9 (49.4)[a]	10.1 (55.6)	10 (72.6)	11.0 (48.2)	12.9 (55.7)	7.2 (17.8)	9.4 (26.5)
$I/s(I)$	15.9 (3.0)	11.5 (2.1)	12.4 (2.2)	23.4 (5.6)	13.7 (1.9)	13.8 (4.8)	12.9 (4.9)
Completeness (%)	95.8 (76.8)	97.7 (85.6)	100 (100)	100 (100)	99.8 (99.8)	94.4 (76.5)	100 (100)
Redundancy	7.9 (5.4)	5.6 (4.1)	5.8 (5.7)	11.4 (11.2)	5.7 (5.4)	4.4 (2.4)	4.2 (4.2)
Refinement							
Resolution (Å)		58.6-1.8		35.8-2.0	36.4-1.8	58.7-1.9	46.6-2.0
R_{work}/R_{free}		0.18/0.23		0.20/0.27	0.19/0.25	0.17/0.22	0.21/0.27
No. atoms							
Protein		4237		4224	4199	4310	4234
Water		689		863	682	556	827
Ligand						46	
Metal ions (Zn)		3		3	-	3	3
Selenium		6		-	-	-	-
B-factor (Å^2)							
Protein		16.89		17.16	16.32	15.11	12.03
Ligands		-		-	-	32.29	-
Water		24.09		20.65	24.88	23.70	18.18
R.m.s. deviations							
Bond length (Å)		0.010		0.011	0.007	0.014	0.011
Bond angles (°)		1.116		1.195	1.049	1.121	1.115
Ramachandran favoured/outliers (%)		98.0/0.0		98.2/0.0	98.6/0.17	97.8/0.19	97.2/0.21
Total number of residues in the AU		537		537	532	541	538
PDB code		2y28		2y2d	2y2c	2y2b	2y2e

[a] Value for the highest resolution shell is shown in parenthesis.

These four regions surround the catalytic zinc ion (Fig. 2*C*). To our knowledge, this structural mobility represents one of the largest, if not the largest, ever reported for a single-domain protein. Utilizing the Dali server (34), the closest structural models of the crystal structure of AmpD are the periplasmic PG amidase AmiD (Z score 17.8, RMSD of 1.9 Å for 135 Cα atoms), the endolysin from *Bacillus subtilis* (Z score 15.5, RMSD of 2.5 Å for 141 Cα atoms), the lambda prophage Ba02 endolysin (PlyL) encoded by the *Bacillus anthracis* genome (Z score 15.1, RMSD of 2.6 Å for 143 Cα atoms) and all the PGRPs from different species, such as PGRP-LE or PGRP-SA from *Drosophila melanogaster* (Z score 14.5, RMSD of 2.4 Å for 138 Cα atoms) or Human PGRP-Iα (Z score 14.4, RMSD of 2.3 Å for 135 Cα atoms). The NMR structure of AmpD appears at the end of the list at position 108 (Z score 13.2, RMSD of 3.5 Å for 159 Cα atoms).

Characteristics of the PG Binding Cleft—The crystals of AmpD turned over the synthetic substrate on soaking (Fig. 3, *A* and *C*). There exists a cavity in AmpD (the glycan-binding site) in which the 1,6-anhydro-*N*-acetylmuramyl moiety is accommodated (Fig. 3*A*). This cavity is connected to a long groove in which the peptide stem is ensconced (the peptide-binding site). The PG-binding site of AmpD, whose general topography is maintained in other PGRPs (35–38), resides in a long cleft whose surface is formed by helix α2 and four loops (β3–3_{10}(1), β4-α1, α2-β5, 3_{10}(4)-α4 and β6-β7) that project above the central β-sheet platform (Fig. 1*B*). The groove is ~26 Å long, with a narrow region near the active site (~9 Å wide) and broader portions at the ends (~12 Å wide at the glycan-binding site and ~16 Å wide at the end of the peptide-binding site). The main differences between PG-binding cleft in AmpD and PGRPs are the entire r2 region (presenting α1 and α2 helices) that is completely different than that observed in PGRPs (in fact this region is strongly stabilized in PGRPs through highly conserved disulfide bridges) and, to a less extent, the r1 region and the 97–107 loop (Fig. 4).

PG Recognition in AmpD—The complex of the 1,6-anhydro-*N*-acetylmuramyl moiety in the active site is stabilized by hydrophobic residues (Fig. 3*C*), constituting the surface of the glycan-binding site. The lactate carboxylate, formed on catalysis within the crystal, is coordinated to the zinc ion, replacing the metal-coordinated water molecule seen in the structure of the native enzyme (supplemental Fig. S1). Three residues (Asn-35, Lys-162, and Tyr-63) are critical in orientation of the 1,6-anhydro-*N*-acetylmuramyl moiety through hydrogen bonds. These interactions are in agreement with reported mutagenesis results indicating that modification of Tyr-63 or Lys-162 resulted in strong attenuation of the AmpD activity (39). The peptide is mainly stabilized by three salt-bridge interactions, while hydrophobic residues (especially Trp-95) build a surface on which the backbone of the peptide stem is accommodated. In addition, hydrogen-bonding interactions are also observed (Fig. 3*C*). Interestingly Arg-71 interacts with diaminopimelate (DAP) moiety (Fig. 3*C*); the presence of an Arg or Asp residue at this position has been reported as critical for DAP or Lys specificity at the third position of the stem peptide in PGRP-SD (40) and PGRP-SA (41), respectively. The three-dimensional structure of AmiD, a periplasmic enzyme of the same amidase_2 family (PF01510), has very recently been described in complex with its substrate (42). Whereas in both AmiD and AmpD a

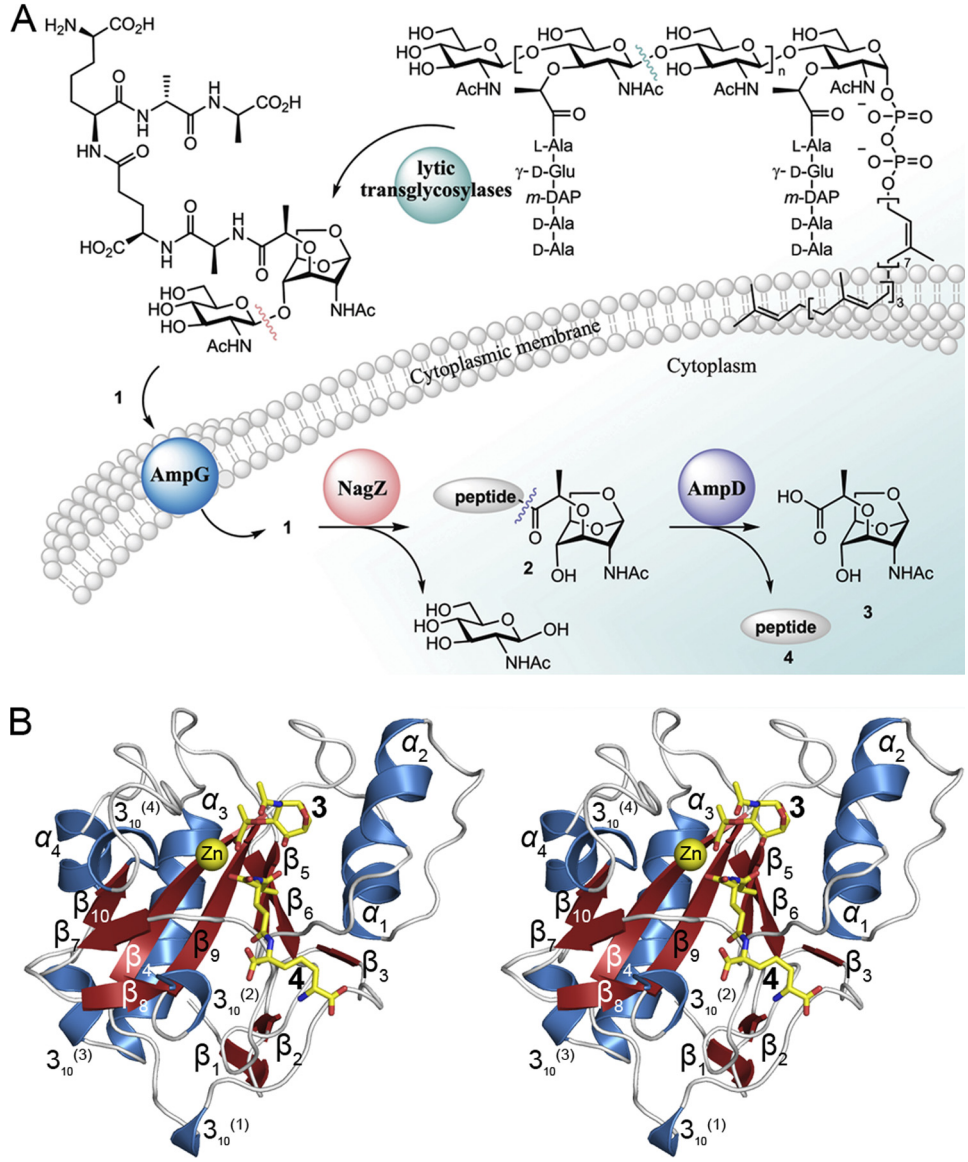

FIGURE 1. **Cell wall recycling and AmpD crystal structure.** *A*, schematic of the early events of cell wall recycling. *B*, stereo view showing three-dimensional structure of AmpD in complex with the reaction products 3 and 4. Secondary structure elements are labeled.

similar structure and protein-ligand interaction pattern are observed for the r4 and the r1 regions; r2 and r3 regions are absent in AmiD (supplemental Fig. S2).

Structural Rearrangements upon Activation—Superimposition of our AmpD in complex with reaction products onto the NMR structure reveals that the latter could not accommodate ligand binding, as the "closed" structure lacks space for both the glycan and peptide moieties of the substrate (Fig. 3, *A* and *B*). In fact, critical residues for binding to the substrate such as Arg-161 and Lys-162, as seen in the x-ray complex, are more than 20 Å away from their corresponding positions in the NMR structure (Fig. 3, *A* and *B*). The foregoing discussion reveals that the NMR structure simply lacks an active site predisposed to binding of the substrate. Hence, the obvious conclusion is that the conformer of AmpD as seen in the NMR structure is that of an inactive enzyme (^{i}AmpD), whereas the x-ray structure is the active conformer (^{a}AmpD). The change of conformation from the ^{i}AmpD to ^{a}AmpD involves large structural rearrangements (in both backbone and side chains), resulting in a significant reorganization of the secondary structural elements in the protein (Fig. 3*D*) and in modification of the intramolecular interaction network. These structural rearrangements intimately entail the regions r2-r4, which are virtually unconnected through space to each other in ^{i}AmpD, but converge to come in close contact with one another in the structure of ^{a}AmpD (Fig. 3, *A* and *B*). This process can best be characterized as an enzyme-activation event. Distinct changes are also observed in the coordination of the catalytic zinc ion (supplemental Fig. S1). We add that the presence of zinc cation is not required to maintain the overall conformation of the enzyme, as the same was observed in both the holo and apoenzyme structures.

The largest changes are observed in the r2 region (an average of 7 Å for 33 Cα atoms) that starts with the ^{39}PPGEFGGP^{46} loop. This region is unique among all the three-dimensional structures of amidase_2 family members reported to date. The nature of the amino acid composition of this loop presents

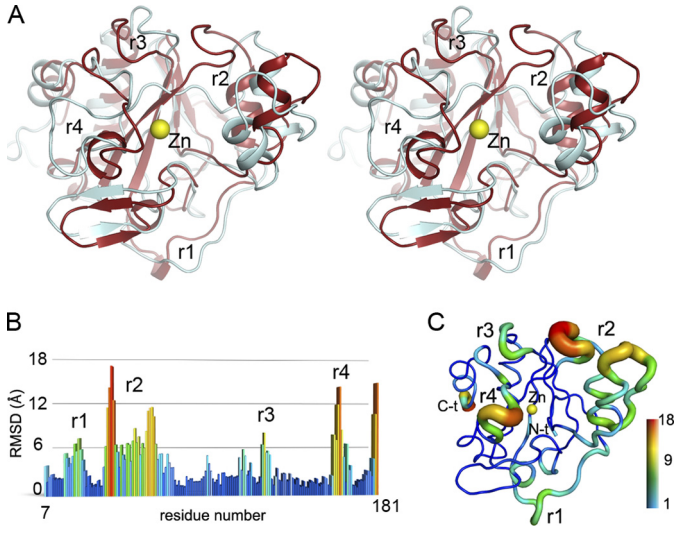

FIGURE 2. **Structural differences between NMR and x-ray structures.** *A*, stereo view of the superimposition of the NMR structure (PDB code 1J3G) in *cyan* and the x-ray structure (this report) in *red*. *B*, root-mean square deviations along the sequence between the NMR structure and the x-ray structure. RMSD values are represented in colors ranging from *blue* (lower RMSD values) to *red* (higher RMSD values). Regions r1–r4 showing the highest structural deviations (4–17 Å) are labeled. The C-terminal tail presenting also large RMSD values was not considered due to the high variability exhibited among the 20 conformers of the NMR PDB file. *C*, tube representation of AmpD showing the largest structural rearrangements between the NMR and x-ray structures. Rearrangements in the backbone of the polypeptide chain are indicated by colors (as in *panel C*) and also by the thickness of the Cα chain that augments with increasing RMSD.

important clues to the structural rearrangement; Gly residues provide flexibility to the stretch of amino acids, and the first two residues (Pro-39, Pro-40) change their amide configurations from *cis* to *trans*, and *trans* to *cis*, respectively, in transition from the inactive to the active states, reminiscent of what is seen during interfacial activation of lipases (43, 44). Furthermore, Glu42 is pivotal in the structure of ^{i}AmpD by making a strong salt-bridge interaction network with an exposed basic patch of positively charged residues (Arg-12, Arg-13, Arg-79, and Arg-80). Interestingly this network is broken in ^{a}AmpD (Fig. 5).

The AmpD enzymes from different bacteria are highly homologous and their structures must be very similar to that of the *C. freundii* AmpD. Therefore, point mutations that inactivate the AmpD from one bacterial species are probably also deleterious in *C. freundii* AmpD. A compilation of inactivation mutations from nine enterobacteria identified 19 residues as sites of inactivating point mutations capable of triggering constitutive β-lactamase expression (45). As reported in the discussion of the NMR structure of AmpD (15), most of these mutations were not located at the active site and therefore the structural explanation of their relevance was rather difficult to assign at the time. However, our structural comparison of ^{i}AmpD and ^{a}AmpD can now explain the relevance of all of these amino acids (supplemental Table S1). In fact, most of these mutations are indeed blocking (i) the structural arrangement required to transition from the inactive to the active conformation, (ii) the salt-bridge interaction network or (iii) the interaction with the substrate in the active conformation (supplemental Table S1). Such inactivating point mutations blocking structural rearrangement required for AmpD activation, further support the existence of both inactive and active states in AmpD.

Conformational Transition between the Inactive and Active States—The conformational transition between the inactive and active states was explored by Targeted Molecular Dynamics (TMD) simulation, which revealed a plausible route to transformation from one conformational state to the other (supplemental Fig. S3 and Movies S2*A* and S2*B*). Within the first 0.5 ns, drastic local rearrangements of α1 and α2 helices from the r2 region are observed, accompanied by conformational changes within the r4 region, corresponding to the loop comprised of β10 and α4 helix. The hinge motion of r2 region involves a rapid swing of both α1 and α2 helices, which then induce conformational rearrangements of the adjacent ^{39}PPGEFGGP^{46} loop, in particular a sliding displacement of the hydrophobic Phe-43 that becomes more exposed to the solvent (0.5 ns). Phe-43 appears to play a key role during the conformational transition (~1 ns) by pulling away Glu-42 out of the tight Arg12-Glu42-Arg79 salt-bridge network. As shown by the sharp increase in distances Glu42···Arg79 and Glu42···Arg12 (Fig. 5), the Glu-42 side chain is displaced rapidly (around 1.0 ns of the simulation) toward its crystallographic position after breaking first the ionic interaction with Arg-12 guanidinium, then dissociating from Arg-79 side chain, while transiently interacting with Arg-80. All together these data provide structural context into how AmpD can experience conformational change between the two states, with a likely modest energy barrier, given the low force constant (lower than 0.06 kcal mol^{-1} Å^{-2}) required to drive the conformation transition in TMD.

Effect of pH on AmpD Structure—The presence of the substrate seems not to be responsible for AmpD activation as we obtained the same three-dimensional structure for the enzyme by itself and in complex with its substrate/products. A difference between the conditions for the two structural determinations (NMR and x-ray) was pH. To see the effect of pH on crystal structure, first, AmpD crystals obtained at pH 6.0 were soaked in buffer at pH 5.5 (that of NMR determination) without any observable effect on crystal quality. Second, we succeeded in growing AmpD crystals at pH 5.5. The AmpD structure at pH 5.5 presented intriguing differences compared with that at pH 6.0 (RMSD. of 0.36 Å for all Cα atoms), all concentrated in the regions involved in activation (supplemental Fig. S4). In addition, the Zn coordination was more similar to that observed in the NMR structure (supplemental Fig. S1). To further explore pH effect on AmpD, we performed extended x-ray absorption fine structure (EXAFS) spectroscopy experiments at different pH values (see "Experimental Procedures"). X-ray absorption spectroscopy (XAS) provides information about the electronic and geometrical structure around the absorbing atom. XAS experiments were performed at different pH values (5.6, 6.0, 7.0, and 8.2) in order to analyze their changes in Zn coordination. In supplemental Table S2, the structural parameters obtained for atoms around Zn are shown. XAS results indicate the existence of three different zinc local structures as a function of the pH of the media. The structure at 7.0 and 8.2 are similar, while the Zn coordination at pH 6.0 is in agreement

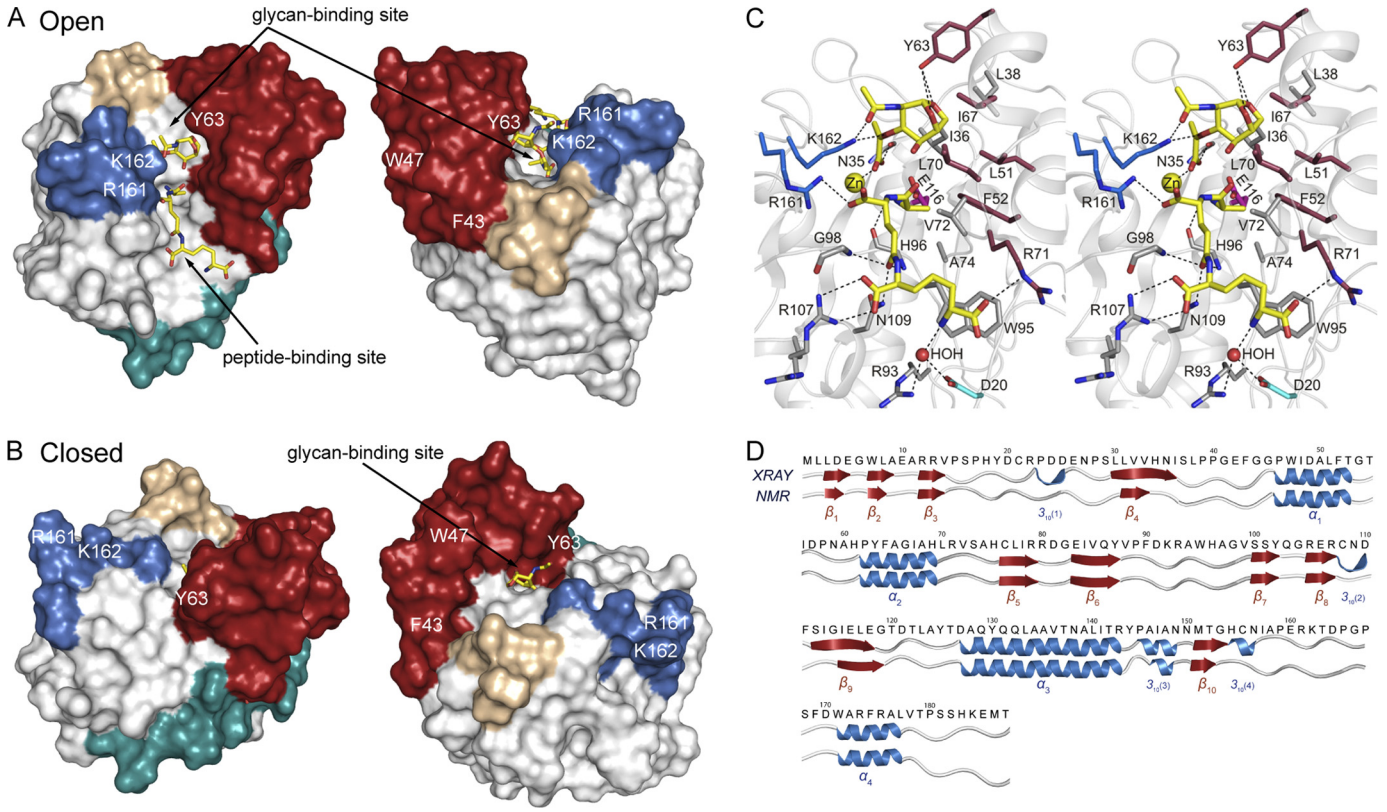

FIGURE 3. **Structural rearrangements upon AmpD activation.** *A*, molecular surface representation of [a]AmpD in complex with the reaction products of compound 2 (*left*, top view; *right*, side view). The region r1 is colored in *cyan*, r2 in *red*, r3 in *brown*, and r4 in *dark blue*. Reaction products seen in the x-ray structure are represented as *capped sticks*. Glycan and peptide-binding sites are labeled. Position of some residues on the surface is indicated. *B*, same perspective as in *panel A* of [i]AmpD with the molecular surface colored as in the previous panel (*left*, top view; *right*, side view). The products of the reaction, as observed in the x-ray structure, have been superimposed for the demonstration of structural clash in the closed conformation of the NMR structure. Despite the fact that the glycan binding cavity is even larger in the NMR structure (solvent accessible volume/surface of 1009 Å^3/628 Å^2 *versus* 738 Å^3/394 Å^2 for the x-ray structure, as calculated by *CASTp* (54), it could simply not accommodate the bicyclic sugar as observed in the x-ray complex. The elongated groove constituting the peptide-binding site is entirely absent in the NMR structure. *C*, details of substrate recognition by AmpD. The view shows the interactions between AmpD and the hydrolyzed substrate. The residues forming the active site are drawn as *capped sticks*. Carbon atoms of the ligand are in *yellow*, while those in the protein are color coded as in *panel A*. Salt-bridges and hydrogen bonds are shown as *dashed lines*.

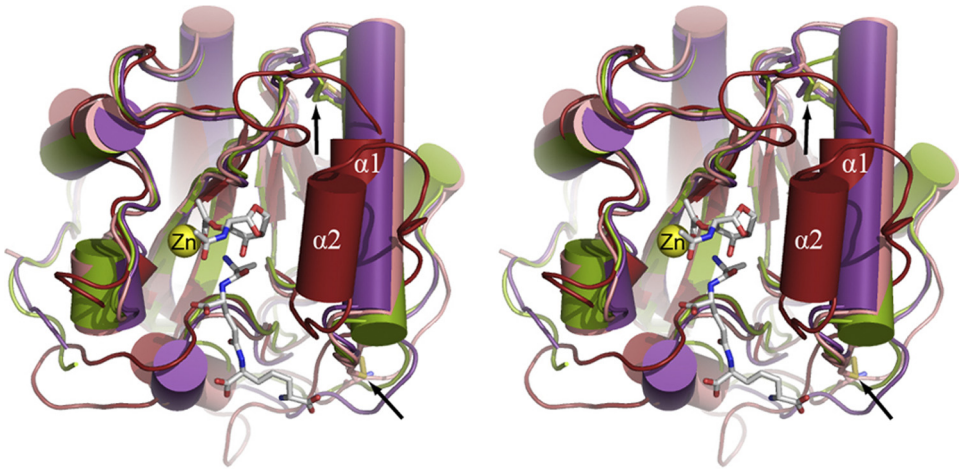

FIGURE 4. **Structural comparison of AmpD and PGRPs.** Superimposition of [a]AmpD structure (*red*) and PGRPs structures (PGRP-SD in *magenta*, PGRP-SA in *green*, and PGRP-Iβ in *salmon*). Reaction products **3** and **4** as seen in the AmpD complex are drawn as *capped sticks*. *Arrows* indicate disulfide bridges present in PGRP structures in the region equivalent to AmpD r2 region.

with the crystal structure ([a]AmpD) and that at pH 5.6 is in agreement with the reported NMR ([i]AmpD) structure. These results further support the different structural results obtained by NMR and x-ray methods.

Mechanistic Implications—The difference of 0.5 pH unit for the two conditions under which the crystals were grown is rather inconsequential. However, the structural changes that we observed argue that the protein inherently enjoys a significant propensity (low energy barrier) for conformational change within regions identified as important for transition between the two extremes of conformational states revealed by the x-ray and NMR structures. Insofar as one structure does not have a

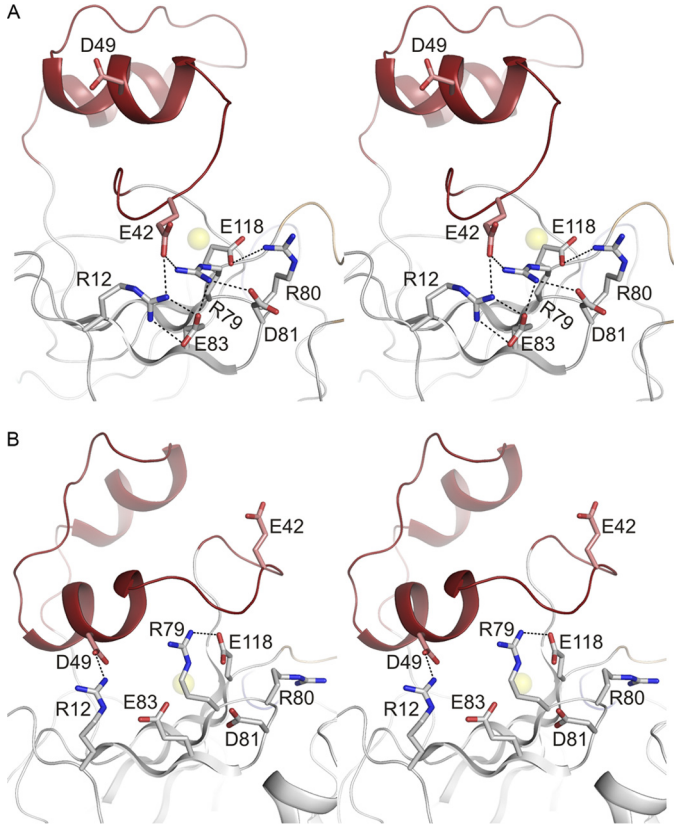

FIGURE 5. **Salt-bridge interactions network in inactive and active conformations of AmpD.** *A*, stereo view of the salt-bridge interactions (*dashed lines*) in ^{i}AmpD. Region r2 is colored in *red*. Residues involved in the network are represented as *capped sticks*. *B*, stereo view of the salt-bridge interactions (*dashed lines*) in ^{a}AmpD. Colors are as in *panel A*. Glu-42 would appear to play a key role in ^{i}AmpD by making strong salt-bridge interactions with Arg-12 and Arg-79, creating an extended salt-bridge interaction network in this region. This network is broken in the ^{a}AmpD in which the Glu-42 side chain merely extends to the solvent, while Arg-12 reinforces the active conformation by making a new salt-bridge interaction with Glu-49 that was 10 Å distant in ^{i}AmpD.

functional active site and represents an inactive AmpD and the other has a fully constituted active site with demonstrated catalytic activity within the crystals, it is compelling to argue that the structural transition represents a heretofore unprecedented mechanism for activation of a zinc peptidase/proteinase. Why such an activation mechanism should be required is not known presently, but we speculate on a reason here.

The crystal structure of AmiD (42), a related peptidoglycan peptidase, lacks most of the structural regions involved in conformational change in AmpD. AmpD is cytoplasmic, whereas AmiD is periplasmic. In light of the fact that the zinc-ion environment that we have determined for ^{a}AmpD is exactly that seen in many disparate active zinc-dependent proteases, it is likely that this enzyme would have adventitious proteolytic activities within the cytoplasm. To shelter the cytoplasm molecules from these adventitious activities an activation mechanism would be beneficial, and might indeed be required. To regulate proteolysis, a common strategy by nature is zymogen activation that typically involves proteolytic removal of a segment of the primary structure to make available the fully constituted active site for its biological function. The zymogen-activation strategy in regulation of function of AmpD is not

TABLE 2
Effect of lipid vesicles on activity of AmpD
Buffer A is 20 mM phosphate, 1.0 mM DTT, pH 7.0. Buffer B is 40 mM bicarbonate, 1.0 mM DTT, pH 7.0.

		K_m	k_{cat}	k_{cat}/K_m
		mM	s^{-1}	$M^{-1}s^{-1}$
Buffer A	Without lipids	1.0 ± 0.1	10.5 ± 0.7	(10.8 ± 0.2) × 10^3
	Lipids (1.5 mg/ml)	1.7 ± 0.1	16.5 ± 1.0	(10.0 ± 0.2) × 10^3
Buffer B	Without lipids	1.2 ± 0.1	6.3 ± 0.1	(5.1 ± 0.3) × 10^3
	Lipids (1.5 mg/ml)	2.0 ± 0.3	11.9 ± 0.5	(6.0 ± 0.4) × 10^3

seen, but the transition between the inactive and active conformations for AmpD could provide the means for such a regulatory mechanism.

The amidase_2 family includes the PGRPs that are highly conserved from insects to mammals (46–49). These enzymes can display specificities for the peptidoglycan of various bacteria and some of them have a Zn^{2+}-binding site that exhibits a related amidase activity (50). Sequence analysis among amidase_2 members reveals that regions that we implicate in the activation mechanism of AmpD (especially r2) are conserved in all bacterial AmpD enzymes and in some intracellular PGRP with peptidase activity, while all related periplasmic or extracellular enzymes do not (supplemental Fig. S7).

The triggering event for transition from the inactive to active conformations for AmpD is presently unknown. While in some Zn-containing carboxypeptidases, the presence of the ligand produce a hinge-bending motion between two subdomains (51), it is likely that in AmpD there might be an allosteric mechanism for the triggering event. For example, we see a patch of positively charged amino acids on the surface of AmpD that might interact with the lipid head groups on the inner leaflet of the cytoplasmic membrane. This patch concentrates most of the AmpD basic residues not involved in ligand binding. Interestingly, this cluster is part of the salt-bridge interaction network (in which the critical Glu-42 is involved) observed in ^{i}AmpD. The presence of basic patches such as this has been associated with membrane sensing and binding in BAR domains, as an example (52, 53). AmpD is a soluble protein, but via this patch of amino acids it might interact with the membrane near the integral membrane permease AmpG (Fig. 1*A*). We have documented that the kinetic parameters are influenced in the presence or absence of lipid constituents. For example, both K_m and k_{cat} are increased in the presence of membrane vesicles made of bacterial lipid extracts (Table 2). The opportunity for multiprotein complexes, for example among AmpG, AmpD, AmpE, and NagZ, or with other proteins, have not been explored, but might serve yet as another means to the triggering of the conformational transition.

In summary, our 1.7 Å resolution x-ray structure clearly shows an open conformation for the bacterial AmpD protein that can accommodate the structures of the substrate for this enzyme. Moreover, the x-ray structure is quite distinct from the previously determined NMR folding for the same enzyme, a structure that does not have an exposed active site and could not bind the substrates. Targeted molecular dynamics also provides insight into how a transition from the inactive NMR structure to the active x-ray one could take place. This unprecedented activation mechanism for AmpD might actually be

more widely present among the intracellular members of the bacterial amidase_2 family of enzymes.

REFERENCES

1. de Pedro, M. A., Donachie, W. D., Höltje, J. V., and Schwarz, H. (2001) *J. Bacteriol.* **183,** 4115–4126
2. Park, J. T., and Uehara, T. (2008) *Microbiol. Mol. Biol. Rev.* **72,** 211–227
3. Cheng, Q., and Park, J. T. (2002) *J. Bacteriol.* **184,** 6434–6436
4. Lee, M., Zhang, W., Hesek, D., Noll, B. C., Boggess, B., and Mobashery, S. (2009) *J. Am. Chem. Soc.* **131,** 8742–8743
5. Jaeger, T., and Mayer, C. (2008) *Cell Mol. Life Sci.* **65,** 928–939
6. Wiedemann, B., Pfeifle, D., Wiegand, I., and Janas, E. (1998) *Drug Resist. Updat.* **1,** 223–226
7. Schleifer, K. H., and Kandler, O. (1972) *Bacteriol. Rev.* **36,** 407–477
8. Doyle, R. J., and Dziarski, R. (2001) in *Molecular Medical Microbiology* (Sussman, M., ed) pp. 137–153, Academic, London
9. Cho, S., Wang, Q., Swaminathan, C. P., Hesek, D., Lee, M., Boons, G. J., Mobashery, S., and Mariuzza, R. A. (2007) *Proc. Natl. Acad. Sci. U.S.A.* **104,** 8761–8766
10. Hoffmann, J. A. (2003) *Nature* **426,** 33–38
11. Royet, J., and Dziarski, R. (2007) *Nat. Rev. Microbiol.* **5,** 264–277
12. Guan, R., and Mariuzza, R. A. (2007) *Trends Microbiol.* **15,** 127–134
13. Dziarski, R., Platt, K. A., Gelius, E., Steiner, H., and Gupta, D. (2003) *Blood* **102,** 689–697
14. Tydell, C. C., Yuan, J., Tran, P., and Selsted, M. E. (2006) *J. Immunol.* **176,** 1154–1162
15. Liepinsh, E., Généreux, C., Dehareng, D., Joris, B., and Otting, G. (2003) *J. Mol. Biol.* **327,** 833–842
16. Hesek, D., Lee, M., Zhang, W., Noll, B. C., and Mobashery, S. (2009) *J. Am. Chem. Soc.* **131,** 5187–5193
17. Kabsch, W. (1993) *J. Appl. Cryst.* **26,** 795–800
18. Leslie, A. G. W. (1992) *Joint CCP4 + ESF-EAMCB Newslett Protein Crystallogra,* p. 26, Daresbury Laboratory, Warrington, UK
19. Evans, P. R. (1993) *in CCP4 Study Weekend* (Sawyer, L., Isaacs, N., and Bailey, S., eds) pp. 114–122, Daresbury Laboratories, Warrington, UK
20. Collaborative Computational Project No 4 (1994) *Acta Crystallogr. D* **50,** 760–763
21. Panjikar, S., Parthasarathy, V., Lamzin, V. S., Weiss, M. S., and Tucker, P. A. (2005) *Acta Crystallogr. D Biol. Crystallogr.* **61,** 449–457
22. Cowtan, K. (1994) *Joint CCP4 + ESF-EAMCB Newslett Protein Crystallography,* p. 31, Daresbury Laboratory, Warrington, UK
23. Perrakis, A., Morris, R., and Lamzin, V. S. (1999) *Nat. Struct. Biol.* **6,** 458–463
24. Jones, T. A., Zou, J. Y., Cowan, S. W., and Kjeldgaard, M. (1991) *Acta Crystallogr. A* **47,** 110–119
25. Emsley, P., and Cowtan, K. (2004) *Acta Crystallogr. D Biol. Crystallogr.* **60,** 2126–2132
26. Adams, P. D., Afonine, P. V., Bunkoczi, G., Chen, V. B., Davis, I. W., Echols, N., Headd, J. J., Hung, L. W., Kapral, G. J., Grosse-Kunstleve, R. W., McCoy, A. J., Moriarty, N. W., Oeffner, R., Read, R. J., Richardson, D. C., Richardson, J. S., Terwilliger, T. C., and Zwart, P. (2010) *H. Acta Crystallogr. D Biol. Crystallogr.* **66,** 213–221
27. Duan, Y., Wu, C., Chowdhury, S., Lee, M. C., Xiong, G., Zhang, W., Yang, R., Cieplak, P., Luo, R., Lee, T., Caldwell, J., Wang, J., and Kollman, P. (2003) *J. Comput. Chem.* **24,** 1999–2012
28. Lee, M. C., and Duan, Y. (2004) *Proteins* **55,** 620–634
29. Schlitter, J., Engels, M., and Krüger, P. (1994) *J. Mol. Graph.* **12,** 84–89
30. Case, D. A., Cheatham, T. E., 3rd, Darden, T., Gohlke, H., Luo, R., Merz, K. M., Jr., Onufriev, A., Simmerling, C., Wang, B., and Woods, R. J. (2005) *J. Comput. Chem.* **26,** 1668–1688
31. Castro, G. R. (1998) *J. Synchrotron Rad.* **5,** 657–660
32. Ravel, B., and Newville, M. (2005) *J. Synchrotron Radiat.* **12,** 537–541
33. Mustre de Leon, J., Rehr, J. J., Zabinsky, S. I., and Albers, R. C. (1991) *Phys. Rev. B Condens. Matter.* **44,** 4146–4156
34. Holm, L., and Rosenstrom, P. (2010) *Nucleic Acids Res.* **38,** W545–W549
35. Guan, R., Roychowdhury, A., Ember, B., Kumar, S., Boons, G. J., and Mariuzza, R. A. (2004) *Proc. Natl. Acad. Sci. U.S.A.* **101,** 17168–17173
36. Kim, M. S., Byun, M., and Oh, B. H. (2003) *Nat. Immunol.* **4,** 787–793
37. Chang, C. I., Ihara, K., Chelliah, Y., Mengin-Lecreulx, D., Wakatsuki, S., and Deisenhofer, J. (2005) *Proc. Natl. Acad. Sci. U.S.A.* **102,** 10279–10284
38. Chang, C. I., Chelliah, Y., Borek, D., Mengin-Lecreulx, D., and Deisenhofer, J. (2006) *Science* **311,** 1761–1764
39. Généreux, C., Dehareng, D., Devreese, B., Van Beeumen, J., Frère, J. M., and Joris, B. (2004) *Biochem. J.* **377,** 111–120
40. Leone, P., Bischoff, V., Kellenberger, C., Hetru, C., Royet, J., and Roussel, A. (2008) *Mol. Immunol.* **45,** 2521–2530
41. Chang, C. I., Pili-Floury, S., Hervé, M., Parquet, C., Chelliah, Y., Lemaitre, B., Mengin-Lecreulx, D., and Deisenhofer, J. (2004) *PLoS Biol.* **2,** E277
42. Kerff, F., Petrella, S., Mercier, F., Sauvage, E., Herman, R., Pennartz, A., Zervosen, A., Luxen, A., Frere, J. M., Joris, B., and Charlier, P. (2010) *J. Mol. Biol.* **397,** 249–259
43. Grochulski, P., Li, Y., Schrag, J. D., and Cygler, M. (1994) *Protein Sci.* **3,** 82–91
44. Brzozowski, A. M., Derewenda, U., Derewenda, Z. S., Dodson, G. G., Lawson, D. M., Turkenburg, J. P., Bjorkling, F., Huge-Jensen, B., Patkar, S. A., and Thim, L. (1991) *Nature* **351,** 491–494
45. Petrosino, J. F., Pendleton, A. R., Weiner, J. H., and Rosenberg, S. M. (2002) *Antimicrob. Agents Chemother.* **46,** 1535–1539
46. Werner, T., Liu, G., Kang, D., Ekengren, S., Steiner, H., and Hultmark, D. (2000) *Proc. Natl. Acad. Sci. U.S.A.* **97,** 13772–13777
47. Liu, C., Xu, Z., Gupta, D., and Dziarski, R. (2001) *J. Biol. Chem.* **276,** 34686–34694
48. Christophides, G. K., Zdobnov, E., Barillas-Mury, C., Birney, E., Blandin, S., Blass, C., Brey, P. T., Collins, F. H., Danielli, A., Dimopoulos, G., Hetru, C., Hoa, N. T., Hoffmann, J. A., Kanzok, S. M., Letunic, I., Levashina, E. A., Loukeris, T. G., Lycett, G., Meister, S., Michel, K., Moita, L. F., Muller, H. M., Osta, M. A., Paskewitz, S. M., Reichhart, J. M., Rzhetsky, A., Troxler, L., Vernick, K. D., Vlachou, D., Volz, J., von Mering, C., Xu, J., Zheng, L., Bork, P., and Kafatos, F. C. (2002) *Science* **298,** 159–165
49. Dziarski, R. (2004) *Mol. Immunol.* **40,** 877–886
50. Wang, M., Liu, L. H., Wang, S., Li, X., Lu, X., Gupta, D., and Dziarski, R. (2007) *J. Immunol.* **178,** 3116–3125
51. Towler, P., Staker, B., Prasad, S. G., Menon, S., Tang, J., Parsons, T., Ryan, D., Fisher, M., Williams, D., Dales, N. A., Patane, M. A., and Pantoliano, M. W. (2004) *J. Biol. Chem.* **279,** 17996–18007
52. Zhu, G., Chen, J., Liu, J., Brunzelle, J. S., Huang, B., Wakeham, N., Terzyan, S., Li, X., Rao, Z., Li, G., and Zhang, X. C. (2007) *EMBO J.* **26,** 3484–3493
53. Reider, A., Barker, S. L., Mishra, S. K., Im, Y. J., Maldonado-Báez, L., Hurley, J. H., Traub, L. M., and Wendland, B. (2009) *EMBO J.* **28,** 3103–3116
54. Dundas, J., Ouyang, Z., Tseng, J., Binkowski, A., Turpaz, Y., and Liang, J. (2006) *Nucleic Acids Res.* **34,** W116–118

Crystal Structures of Bacterial Peptidoglycan Amidase AmpD and an Unprecedented Activation Mechanism

Cesar Carrasco-López, Alzoray Rojas-Altuve, Weilie Zhang, Dusan Hesek, Mijoon Lee, Sophie Barbe, Isabelle André, Pilar Ferrer, Noella Silva-Martin, German R. Castro, Martín Martínez-Ripoll, Shahriar Mobashery and Juan A. Hermoso

J. Biol. Chem. 2011, 286:31714-31722.
doi: 10.1074/jbc.M111.264366 originally published online July 20, 2011
